Pore Structure−Chemical Composition Interactions of New High Surface Area Manganese Based Mesoporous Materials. Materials Preparation, Characterization, and Catalytic Activity

4 AUTHORS, INCLUDING:

Constantinos Salmas
National Technical University of Athens

32 PUBLICATIONS **424** CITATIONS

SEE PROFILE

V. N. Stathopoulos
Technological Educational Institute of Sterea…

63 PUBLICATIONS **359** CITATIONS

SEE PROFILE

Pore Structure−Chemical Composition Interactions of New High Surface Area Manganese Based Mesoporous Materials. Materials Preparation, Characterization, and Catalytic Activity

Constantinos E. Salmas,[†] Vassilis N. Stathopoulos,[‡] Philippos J. Pomonis,[‡] and George P. Androutsopoulos*,[†]

Department of Chemical Engineering, Section II, Chemical Process Engineering Laboratory, National Technical University of Athens, 9 Heroon Polytechniou Street, GR 157 80 Athens, Greece, and Department of Chemistry, Section of Industrial and Food Chemistry, Laboratory of Industrial Chemistry, University of Ioannina, GR 451 10 Ioannina, Greece

The present article deals with pore structure−chemical composition interactions of new high surface area manganese based porous mixed oxides (MANPOs). These mixed oxidic materials were prepared by the dropwise addition of a solution containing metal nitrate into an acetonic solution containing the trinuclear complex of manganese $[Mn_3O(CH_3COO)_6(pyr)_3]ClO_4$, which is water sensitive. The CPSM model (corrugated pore structure model) was employed in pore structure investigations of the MANPO materials containing Al, Fe, La, La + Ce, and La + Sr. Successful CPSM simulations of nitrogen sorption hysteresis loops for the MANPO solids enabled the evaluation of intrinsic pore size distributions (PSDs) and tortuosity factors. The latter vary over the approximate range $\tau_{CPSM} = 3.0−5.7$ (i.e. $\tau_{CPSM} \approx 3$ for materials containing Al or Fe and $\tau_{CPSM} = 4.7−5.7$ for those containing La, La + Ce, or La + Sr). These values are typical of porous catalysts and are higher than those reported for MCM-41 materials (ca. $\tau_{CPSM} = 1.00−2.35$) and anodic aluminum oxide films (e.g. $\tau_{CPSM} = 2.60$). The BET surface areas of the MANPO materials vary over the approximate range 180−900 m²/g, being higher than those reported for manganese oxide mesopore solids (MOMS), for example 59−170 m²/g. Intrinsic PSD predictions for the MANPO solids are of bimodal type with mean pore sizes systematically higher than the respective mean hydraulic diameters. The addition of Fe and La + Ce caused a PSD shift toward the micropore region. Such MANPO materials are amorphous after heating to 500 °C (except for the ones containing Fe) and extremely efficient catalysts for redox reactions such as lean de-NO$_x$ applications and NO−CO conversion, probably because of the extremely high dispersion of separate nanophases into the solid.

1. Introduction

1.1. General. A number of significant applications stress the importance of synthesizing high surface area mesoporous manganese based solids. The latter materials are employed in the catalysis of oxidation reactions taking place at milder temperature conditions than those for reactions catalyzed by noble metals.[1,2] Manganese solids can also be used for the production of aqueous and nonaqueous batteries (either regenerable or nonregenerable type).[1,2] A comprehensive review of various preparation procedures for Manganese catalysts is provided in ref 1 with special reference to the preparation of high surface area mesoporous manganese solids.

1.2. Catalytic Applications of Manganese Oxides. Methane and butane oxidation on oceanic manganese nodules showed a better catalytic activity than that of a commercial Pt−Al₂O₃ catalyst and demonstrated that manganese oxides possess satisfactory oxidation properties and offer the possibility of using these and similar materials in catalytic processes for the removal of volatile organic compounds (VOCs) as well as gaseous pollutants from combustion gases.[3,4] The combination of manganese oxide with other transition metals results in the formation of active catalytic materials suitable for the oxidation of a spectrum of VOC compounds. Moreover, the required process temperatures are lower than those for the corresponding catalytic materials containing noble metals.[5] Additional applications of manganese based catalysts are (i) benzene oxidation,[6] (ii) photocatalytic conversion of 2-propanol to acetone and the decomposition of halogenated hydrocarbons,[7−9] (iii) selective catalytic reduction of NO in NH₃ or hydrocarbons for the development of pollution abatement technologies against NO$_x$,[10] and (iv) oxidation of cyclohexane into cyclohexanone and hexane into hexanol isomers (i.e. 1-, 2-, 3-).[11]

In most of the abovementioned examples the oxidative manganese materials are nonporous with a low specific surface area (i.e. <10 m²/g). It is, thus, important for the catalytic behavior and hence the development of the

† National Technical University of Athens.

‡ University of Ioannina.

(1) Stathopoulos, V. N.; Petrakis, D. E.; Hudson, M.; Falaras, P.; Neophytides, S. G.; Pomonis, P. J. *Characterization of Porous Solids-V;* Unger, K. K., Kreysa, G., Baselt, J. P., Eds.; Elsevier: Amsterdam, 1999, p 593.

(2) Stathopoulos, V. N.; Belessi, V. C.; Costa, C. N.; Neophytides, S.; Falaras, P.; Efstathiou, A. M.; Pomonis, P. J. *Studies of Surface Catalysis;* Corma, A., Melo, F. V., Mentioroz, S., Fierro, J. L. G., Eds.; Elsevier: Amsterdam, 2000; Vol. 130, p 1529.

(3) Weisz, P. B. *J. Catal.* **1968**, *10*, 407.

(4) Orthmer, K. *Encyclopedia of Chemical Technology*, 4th ed.; Plenum Press: New York, 1991; Vol. 15, pp 1044−1045.

(5) Luo, T.; Suib, S. *J. Phys. Chem. B* **1997**, *101*, 10403.

(6) Luo, T.; Zhang, Q.; Huang, A.; Suib, S. L. *Microporous Mesoporous Mater.* **2000**, *35−36*, 209.

(7) Cao, H.; Suib, S. L. *J. Am. Chem. Soc.* **1994**, *116*, 5334.

(8) Chen, J.; Lin, J.-C.; Purohit, V.; Cutlip, M. B.; Suib, S. L. *Catal. Today* **1997**, *33*, 205.

(9) Lin, J.-C.; Chen, J.; Suib, S. L.; Cutlip, M. B.; Freihaut, J. D. *J. Catal.* **1996**, *161*, 659.

(10) Kapteijn, F.; Langeveld, D-v. A.; Mouljin, J. A.; Andreini, A.; Vuurman, M. A.; Turek, A. M.; Jehng, J-M.; Wachs, I. E. *J. Catal.* **1994**, *150*, 94.

(11) Tian, Z. R.; Tong, W.; Wang, J. Y.; Duan, N. G.; Krishnan, V. V.; Suib, S. L. *Science* **1997**, *267*, 926.

corresponding application to synthesize manganese containing materials with high surface area.

1.3. Pore Structure Evaluation. The addition of cations modifies the catalytic activity of manganese based catalysts and causes a pore structure change. Therefore, the study of cation addition–mesopore structure interactions is a worthwhile research target. Prior to the presentation of the experimental results and pore structure evaluation, a brief recapitulation and a critical discussion of both newly reported (i.e. CPSM, corrugated pore structure model) and conventional methods of surface area (SSA) and pore size distribution (PSD) determination will be presented.

1.3.1. Critical Discussion of Methods for Pore Structure Analysis. *Surface Area and Pore Size Distribution.* BET theory provided over several decades the dominant method[12,13] for pore surface area determination, despite the simplified assumptions that are involved and the ambiguity accruing from the choice of the linear part of the BET plot. Two BET variants have been proposed in the original publication of Brunauer et al.[5] The relevant formula for multilayer adsorption reads

$$P/(n_a(P_0 - P)) = (1/n_m C) + ((C - 1)/n_m C)(P/P_0) \quad (1)$$

where (n_a) is the amount (μmols/g) of gas adsorbed at relative pressure (P/P_0), (n_m) is the monolayer capacity (i.e. μmols/g), and C is the BET constant. The BET formula for monolayer adsorption[14] (Langmuir form), applicable in cases of narrow mesopores (i.e. approaching the upper limit of the micropore region, ca. 2 nm) or wider micropores (i.e. 1.5–2 nm),[15] is given by

$$((P/P_0)/n_a) = (1/n_m C) + (1/n_m)(P/P_0) \quad (2)$$

It should be mentioned that for pure physical adsorption the acceptable range of the C constant variation is approximately $20 < C < 200$, since C is related to the enthalpy of adsorption and provides information for the magnitude of the adsorbent–adsorbate energy of interaction.[12–14,16]

The application of the traditional methods for PSD evaluation from gas sorption data encounters the dilemma of selecting either one or the other branch of the hysteresis loop, because markedly different results are obtained when using data of one or the other branch. For instance, cumulative specific surface areas (CSSAs) computed from these methods, by using either adsorption or desorption data, are rarely in agreement between themselves or with the pertinent BET surface area estimates.

Moreover, the methods under consideration do not provide any information on pore structure complexity (e.g. pore tortuosity), since they are based on the simplified model of "bundle of parallel, independent, cylindrical, open ended pores". The CPSM,[17,18] proposed recently, is intended to overcome the abovementioned problems and provides for intrinsic PSD and tortuosity factor predictions via the simulation of gas sorption hysteresis loops. As regards the conventional methods for PSD evaluation from gas sorption data, a number of similar, in structure and performance, methods are applied over several decades. The most frequently applied method is that of Barrett, Joyner, and Halenda (BJH).[19] However, as discussed in ref 17, the Roberts method[20] is equally applicable and is generally considered as a reliable representative of the classical procedures of PSD evaluation.

Diffusion and Pore Structure Tortuosity. The physical characterization of mesoporous manganese solids apart from the specific surface area and intrinsic pore size distribution data requires the knowledge of the total porosity (ϵ) (i.e. ratio of total pore volume and overall volume of particle, v/v) and the tortuosity factor (τ). These pore structure properties correlate, via eq 3, the binary diffusivity $D_{AB}(D_{mean})$ of two counterdiffusing species A and B, through a straight cylindrical pore of mean pore size D_{mean}, with the effective diffusivity D_e of the same species based on the cross-sectional area of a homogeneous porous particle. Thus,

$$D_e = \epsilon D_{AB}(D_{mean})/\tau \quad (3)$$

Porosity can be routinely measured by carrying out particle density determinations, that is, bulk density via mercury displacement and true (skeletal) density via pore filling with He. Tortuosity factor evaluation can be accomplished through eq 3 if $D_{AB}(D_{mean})$, ϵ, and D_e, are known.

For a binary gas mixture diffusing in a porous solid at constant pressure, the combined diffusivity D_{AB} is given[21] by

$$\frac{1}{D_{AB}} = \frac{1}{D_K} + \frac{1}{D_m}\left[1 - \left(1 + \frac{J_B}{J_A}\right)Y_A\right] \quad (4)$$

where D_K is the Knudsen diffusivity, D_m is the molecular diffusivity for gaseous systems, J_A and J_B are the fluxes of components A and B, and Y_A is the mole fraction of component A.

Obviously, for equimolar counterdiffusion $J_A = -J_B$. Thus,

$$\frac{1}{D_{AB}} = \frac{1}{D_K} + \frac{1}{D_m} \quad (5)$$

Equations 4 and 5 are valid under the condition that the surface diffusivity (i.e. the flux from transport through the physically adsorbed gas layer) on the pore surface is negligible.

The Knudsen diffusivity may be computed from the expression[21]

$$D_K \text{ (cm}^2\text{/s)} = 9700\left(\frac{D_{mean}}{2}\right)\left(\frac{T}{M}\right)^{1/2} \quad (6)$$

where D_{mean} is the mean pore diameter in centimeters, [T] is in kelvin, and M is the molecular weight of the diffusing species. D_K for each species does not depend on either composition or total gas concentration because in the Knudsen regime each species diffuses independently. In cases where the Knudsen diffusion is not important, $D_{AB} = D_m$ and eq 3 assumes the form

(12) Davis, B. H. *Appl. Catal.* **1984**, *10*, 185.
(13) Gregg, S. J.; Sing, K. S. W. *Adsorption Surface Area and Porosity*, 2nd ed.; Academic Press: New York, 1982.
(14) Brunauer, S.; Emmett, P. H.; Teller, E. *J. Am. Chem. Soc.* **1938**, *60*, 309.
(15) Rouquerol, F.; Rouquerol, J.; Sing, K. *Adsorption by Powders and Porous Solids*; Academic Press: New York, 1999.
(16) Serwicka, E. M. *Catal. Today* **2000**, *56*, 335.
(17) Androutsopoulos, G. P.; Salmas, C. E. *Ind. Eng. Chem. Res.* **2000**, *39*, 3747.
(18) Androutsopoulos, G. P.; Salmas, C. E. *Ind. Eng. Chem. Res.* **2000**, *39*, 3764.

(19) Barrett, L. P.; Joyner, L. G.; Halenda, P. P. *J. Am. Chem. Soc.* **1951**, *73*, 373.
(20) Roberts, B. F. *J. Colloid Interface Sci.* **1967**, *23*, 266.
(21) Ruthven, D. M. *Principles of Adsorption and Adsorption Processes*; J. Wiley & Sons: New York, 1984; pp 127.

$$D_e = \epsilon D_m / \tau \qquad (7)$$

Binary diffusion coefficients D_m for gaseous systems can be calculated from the Chapman−Enskog equation.[21] For a binary gas mixture

$$D_m \ (cm^2/s) = [0.00158\,T^{3/2}(1/M_1 + 1/M_2)^{1/2}]/$$
$$[P\sigma^{1/2}\Omega(\epsilon/kT)] \quad (8)$$

where M_1 and M_2 are the molecular weights, P is the total pressure in atmospheres, $\sigma_{12} = 0.5(\sigma_1 + \sigma_2)$ is the collision diameter from the Lennard-Jones potential, expressed in angstroms, and Ω is a function of ϵ/kT, where $\epsilon = (\epsilon_1\epsilon_2)^{0.5}$ is the Lennard-Jones force constant and k is the Boltzmann constant.

The determination of D_e presents the chief difficulty due to the complexity of experimental procedures and the uncertainties inherently involved in the theoretical models used in the analysis of experimental results. A number of experimental techniques can be applied for the evaluation of D_e. Some of them are the Wicke and Kallenbach experiment,[21] reaction kinetic studies,[22] and gas chromatography techniques.[23]

To avoid the execution of diffusion measurements and thus make the evaluation of D_e convenient, a new method (i.e. CPSM−tortuosity[15]) was recently proposed.[24] This method employs an empirical correlation (eq I-6) whose formulation is based on the CPSM−nitrogen[17,18] predictions for both intrinsic PSD and nominal pore length parameter (N_s) values.

1.3.2. Corrugated Pore Structure Model. The corrugated pore structure model (CPSM) is a unified theory enabling the simulation of nitrogen sorption[17,18] and mercury porosimetry hysteresis[25,26] phenomena as well as the prediction of pore structure tortuosity factors. Due to the extensive use of the CPSM that will be made in the present work, a brief outline of the various CPSM variants is presented.

CPSM−Nitrogen Model. The CPSM−nitrogen model[17] is a statistical model simulating the gas sorption hysteresis phenomena, predicts a single PSD by curve fitting the entire sorption hysteresis loop, and is based on a corrugated pore structure configuration. The latter is envisaged to be composed of a sequence of N_s cylindrical pore segments of constant length and distributed diameter. The symbol N_s stands for a statistical nominal pore length. The development of the CPSM−nitrogen model is based on a number of assumptions: the physical multilayer adsorption on the surface of the corrugated pore as described by a modified Halsey equation (eq I-1) and the capillary condensation according to the Kelvin equation (eq I-2).

The condensation is assumed to originally occur preferably on a cylindrical interface at the narrowest segment and then proceeds through a hemispherical one, whereas evaporation proceeds preferably through a hemispherical interface geometry. Following a statistical analysis of the envisaged physical steps taking place within the corrugated pore, the pertinent formulas have been developed.[17] The analytical expressions of the CPSM are

(22) Furimsky, E.; Massoth, F. E. *Catal. Today* **1999**, *52*, 381.

(23) Santos, À.; Bahamonde, A.; Avila, P.; Garæia-Ochoa, F. *Appl. Catal.* **1996**, *10*, 299.

(24) Salmas, C. E.; Androutsopoulos, G. P. *Ind. Eng. Chem. Res.* **2001**, *40*, 721.

(25) Androutsopoulos, G. P.; Salmas, C. E. *Chem. Eng. Commun.* **1999**, *176*, 1.

(26) Androutsopoulos, G. P.; Salmas, C. E. *Chem. Eng. Commun.* **2000**, *181*, 137.

Table 1. Sample Notation and Metal Ratios at Synthesis of Manganese Based Oxides

material	cation ratio	
VAL-21	Mn/Al	0.85
VFE-21	Mn/Fe	0.85
VL-51	Mn/La	1.70
VLCMN-1	Mn/La/Ce	0.85:0.5:0.5
VLSMN-1	Mn/La/Sr	0.85:0.5:0.5

presented in eqs (I-3)−(I-5). Various applications covering the entire spectrum of hysteresis loop types according to the IUPAC classification have been worked out.[18,27]

CPSM−Tortuosity Model. This model consists of an empirical correlation (eq I-6) that is based on CPSM−nitrogen predictions of intrinsic pore size distribution and nominal pore length (i.e. N_s) data. The CPSM−tortuosity model enables realistic predictions of pore structure tortuosity factors in satisfactory agreement with relevant literature data.[28]

CPSM−Mercury Model. The corrugated pore configuration has also been used to formulate mathematical relationships (eqs (II-1)−(II-6)) simulating mercury porosimetry (MP) hysteresis observations (e.g. CPSM−mercury[24]). Similar correlations have been developed simulating MP hysteresis loop scanning data and enabling the definition of pore structure tomography concepts.[26,29]

Intrinsic Pore Size Distribution. A family of bell shaped distribution functions (BSDs) was chosen as the intrinsic pore number distribution $f_r(b_r, D)$ (eq III-2), to facilitate the application of the CPSM both for simulating experimental gas sorption and mercury porosimetry hysteresis data and evaluating tortuosity factors. The respective intrinsic pore number distribution $F(D)$ (eq III-1) appearing in the CPSM equations can be derived by combining a set of (n) f_r-type PSDs. The mathematical form of the BSD enables the analytical integration of the integrals appearing in the CPSM−nitrogen and CPSM−mercury models.

1.4. Scope. The scope of the present communication is to investigate the effect of metal (e.g. Al, Fe, La, La + Ce, and La + Sr) addition during synthesis of the manganese solids on pore structure using the CPSM for pore structure analysis and tortuosity factor evaluation. The CPSM−nitrogen variant will be employed in the analysis of nitrogen sorption hysteresis data while a performance comparison of the CPSM with the pertinent conventional methods, that is, BET for surface area determination and Roberts for PSD evaluation, will be carried out. Moreover, the intrinsic PSD and N_s data, as explained above, will be employed for the prediction of tortuosity factors of the materials under examination. Supplementary information on materials preparation, surface and texture characterization, and catalytic activity effectiveness is also presented.

2. Experimental Section

2.1. Manganese Based Porous Oxides (MANPOs) Preparation. Synthesis of the manganese based porous mixed oxides was based on the hydrolysis of trinuclear manganese complex $[Mn_3O(CH_3COO)_6(pyr)_3]ClO_4$ in the presence of metals such as La **(VL-51)**, Al **(VAL-21),** Fe **(VFE−21)**, La + Ce **(VLCMN-1)**, and La + Sr **(VLSMN-1)**. The Mn/metal(s) ratio during hydrolysis can be seen in Table 1. All samples were thermally treated at 300 °C for 4 h in ambient air. Details of the synthesis procedure

(27) Salmas, C. E.; Androutsopoulos, G. P. *Appl. Catal., A* **2000**, 5412.

(28) Satterfield, C. N. *Mass Transfer in Heterogeneous Catalysis;* M.I.T. Press: London, 1970; pp 37, Figure 1.5.

(29) Androutsopoulos, G. P.; Salmas, C. E. *Chem. Eng. Commun.* **2000**, *181*, 179.

Table 2. Physicochemical Characteristics of Mn Based Mixed Oxide Materials

property	calcination T (°C)	Mn–Al–O	Mn–La–O	Mn–La–Ce–O
BET (m²/g)	300	711	247	170
	500	310	166	122
crystal structure/XRD	500	amorphous	amorphous	amorphous
Mn/A in hydrolysis		1.70:1	0.85:1	0.85:0.5:0.5
surface composition/XPS	500	0.28:0.11:0.61	0.33:0.05:0.62	0.18:0.11:0.28:0.53
roughness/AFM (nm)	300	9.76	13.35	–
particle size/AFM (nm)	300	20	10–15	–
fractal dimension/AFM	300	2.22	2.29	–

can be found elsewhere[1,30,31] and are as follows: The trinuclear manganese complex [$Mn_3O(CH_3COO)_6(pyr)_3$]ClO_4 was prepared[1] according to the original report of its synthesis.[30]

Briefly, 2 g of $Mn(CH_3COO)_2 \cdot 4H_2O$ (6.15 mmol) was dissolved in a mixture of 20 mL of ethyl alcohol, 3 mL of pyridine, and 12 mL of glacial acetic acid. In this mixture 1.14 g (3.15 mmol) of N-^{n}Bu$_4$MnO$_4$ was added under vigorous stirring, where N-^{n}Bu$_4$-MnO$_4$ is tetrabutyl permanganate prepared by mixing aqueous solutions of $KMnO_4$ and N-^{n}Bu$_4$Br. Addition of 0.69 g (5.65 mmol) of $NaClO_4$ resulted in the precipitation of a brown mass of the complex that was subsequently filtered and washed with acetone.

The trinuclear complex, henceforth referred to as Mn$_3$, is readily soluble in warm acetone but instantly hydrolyzed in water. A weighted amount of Mn$_3$ was dissolved in acetone and put in a three-neck spherical flask, equipped with a reflux system used to avoid the escaping of acetone vapor. Then, an aquatic solution of the metallic ions in its nitrate form was added dropwise into the acetonic solution kept at 50 °C. In a typical example, in 250 mL of Mn$_3$/acetonic solution containing 0.01 mol of Mn$_3$, 250 mL of Al(NO$_3$)$_3$/H$_2$O solution (0.141 M) was added dropwise and slowly during 2 h. Then the obtained precipitate was filtered, dried at room temperature, and fired at 300 and 500 °C under atmospheric conditions. Samples prepared in this way are in Table 2 with some of their characteristic properties. Be aware that not all the amount of heterocations in the solution is necessarily incorporated into the solids, as shown below.

2.2. Surface and Textural Characterization of the Solids. The surface composition of the materials obtained was checked using X-ray photoelectron spectroscopy (XPS). The powders were pressed firmly into carved stainless steel holders so that they could be introduced into the ultrahigh vaccum (UHV) chamber (base pressure 8×10^{-10}). The analysis chamber was equipped with a hemispherical analyzer (SPECS LH-10) and a twin-anode X-ray gun. The unmonochromatized Mg Kα line at 1253.6 and a constant pass energy mode (97 eV) for the analyzer were used for the analysis measurements. The calculations of the various component compositions of such solids shown in Table 2 were based on the spectra of the Mn 2p, Al 2p, Fe 3p, La 4d, and O 1s photoelectrons.

The texture and morphology of the materials were investigated by atomic force microscopy (AFM Nanoscope III, Digital Instruments) in the tapping mode. Observations were performed on thin films of these materials deposited on microscope glass slides by solvent evaporation of aqueous dispersions (2 g L^{-1}), homogenized by ultrasounds (30 min). Typical three-dimensional images are shown in Figure 1. The Mn–Al–O and Mn–La–O films are composed of large domains of features of different heights, probably resulting from a rather random particle deposition. On the contrary, for the Mn–Fe–O films, we observed the presence of a more robust and organized structure, which consists of well-defined rocks of different sizes on the top of a continuous background. The grain size analysis revealed that the grain diameter of the lanthanum containing Mn oxide is significantly lower than those of the corresponding aluminum and iron ones (Table 2). Furthermore, the roughness analysis indicated that the standard deviation of the difference between the highest and lowest points (rms), which directly reflects the height of surface features, is significantly higher in the case of the Mn–Fe oxide. Finally, the geometric complexity of the material surfaces was evaluated by a more detailed fractal analysis and the results are indicated in Table 2.[1]
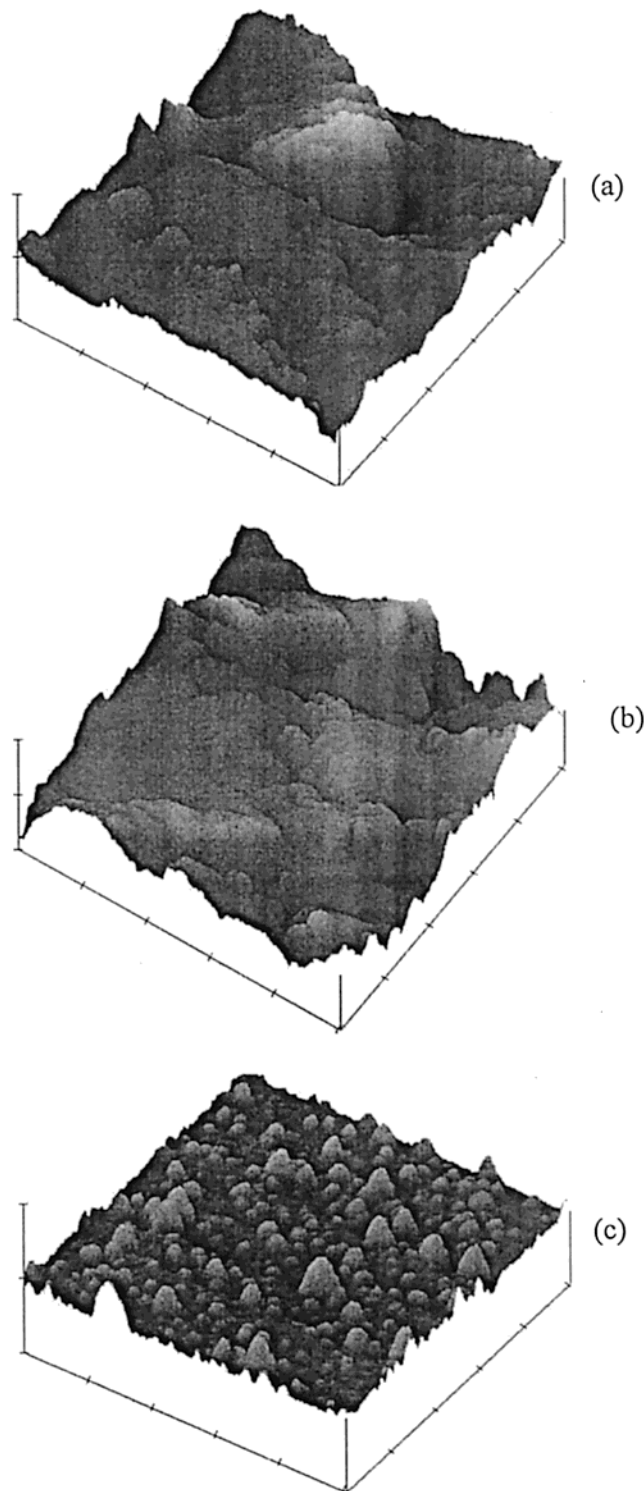
(30) Vincent, J. B.; Chang, H. R.; Folting, K.; Huffman, J. C.; Christou, G.; Hedrikson, D. N. *J. Am. Chem. Soc.* **1987**, *109*, 5703.

(31) Stathopoulos, V. N. Ph.D. Thesis, University of Ioannina, Greece, 2001 (in Greek).

Figure 1. AFM images of (a) Mn–Al–O, (b) Mn–La–O, and (c) Mn–Fe–O solid.

X-ray diffraction analysis showed that such MANPO solids are predominantly amorphous up to 500 °C and only the materials

Table 3. CPSM Fitting Parameters of Nitrogen Sorption Hysteresis Loops for Manganese Based Mesoporous Materials

specimen	V_g(max) (cm³(STP)/g)	N_s[a]	parameters of the intrinsic pore segment number distribution $F(D)$						Kelvin[b] parameters		parameters of t (nm), eq I-1	
			b_1	b_2	w_1	w_2	P_{ce}/P_0	(P/P_0)(max)	$\cos\theta_c$	$\cos\theta_h$	m	n
VAL-21; Mn/Al = 0.85	357.21	10	−100	−30	7	1	0.370	0.945	0.45	0.45	0.17	0.38
VFE−21; Mn/Fe = 0.85	104.94	3.2	−90	−16	4	1	0.27	0.954	0.70	0.70	0.20	0.43
VL-51; Mn/La = 1.70	187.26	20	−60	−	1	−	0.46	0.971	0.60	0.60	0.16	0.45
VLCMN-1; Mn/La/Ce = 0.85:0.5:0.5	78.68	3.4	−200	−14	6	1	0.25	0.981	0.50	0.50	0.18	0.45
VLSMN-1; Mn/La/Sr = 0.85:0.5:0.5	204.23	6	−70	−16	6	1	0.35	0.98	0.80	0.80	0.06	0.38

[a] CPSM nominal pore length. [b] As defined by eq 11.[1]

Table 4. Manganese Based Mesoporous Materials. Specific Surface Areas Obtained by Using BET, CPSM-nitrogen and Roberts Methods

specimen	$S_{BET(mu)}$ (m²/g)	$P/P_{0(mu)}$ range	$C_{BET(mu)}$	$S_{BET(mo)}$ (m²/g)	$P/P_{0(mo)}$ range	$C_{BET(mo)}$	S_{CPSM} (m²/g)	$S_{Ro(co)}$ (m²/g)	$S_{Ro(ev)}$ (m²/g)
VAL-21; Mn/Al = 0.85	741	0.1−0.25	75	**902**	0.04−0.11	41	**902**	343 (−62%)	428 (−53%)
VFE−21; Mn/Fe = 0.85	**201**	0.2−0.44	20	**202**	0.03−0.08	51	**201**	139 (−31%)	159 (−21%)
VL-51; Mn/La = 1.70	**251**	0.02−0.09	90	314	0.05−0.09	43	**251**	148 (−41%)	235 (−6%)
VLCMN-1; Mn/La/Ce = 0.85:0.5:0.5	170	0.06−0.18	60	**183**	0.02−0.08	65	**181**	88 (−51%)	106 (−41%)
VLSMN-1; Mn/La/SR = 0.85:0.5:0.5	**212**	0.00−0.09	305	232	0.01−0.07	181	**211**	172 (−18%)	254 (+20%)

[a] Percent deviation from S_{BET} (values printed in bold).

containing iron show crystallites of Fe_2O_3 and Mn_2O_3,[1,31] as indicated for typical samples in Table 2.

2.3. Nitrogen Sorption Measurements. The specific surface areas and the pore size distributions of the samples were determined by a Fisons SORPTOMATIC 1900 volumetric adsorption−desorption apparatus, using nitrogen as adsorbate at 77.4 K. Prior to the determination of adsorption−desorption isotherms, the samples were degassed at 200 °C under a 5×10^{-2} mbar vacuum for 12 h. The specific surface area determination of the samples was accomplished by applying the BET theory for both multilayer ($BET_{(mu)}$) and monolayer ($BET_{(mo)}$) adsorption and using the respective linear part over the P/P_0 intervals indicated in Table 4. A close-packed BET monolayer, with a_m(N_2) = 0.162 nm² at 77.4 K, was assumed.

3. Results and Discussion

3.1. Nitrogen Sorption Hysteresis. Nitrogen adsorption−desorption runs were carried out at 77.4 K using the MANPO samples of Table 1. The sorption hysteresis experimental data (points) and their CPSM simulation (solid line through the points) are provided in Figure 2. The configuration of these loops is more or less that of H_2-type of the IUPAC classification with VAL-21 and VL-51 being the most typical examples. As seen from Figure 2, CPSM fitting has been quite successful. The relevant parameters for all MANPO samples are presented in Table 3.

In four out of five cases a bimodal intrinsic pore size distribution (i.e. two b values were considered, Table 3) was required to obtain a satisfactory fit. The nominal pore length parameter (N_S) assumed values ranging approximately from 3 to 20, indicating the presence of enhanced pore structure tortuosity in the MANPO samples. The fitting of VAL-21 was obtained for a $\cos\theta$ value less than $\cos\theta_c = \cos\theta_h < 0.5$, indicating the presence of limited microporosity that will be assessed from the location of the intrinsic PSD. For the rest of the MANPO materials, $\cos\theta$ varies over the approximate range $\cos\theta = 0.5−0.8$, indicating the presence of a pseudo-hemispherical (becoming cylindrical in the limit) liquid nitrogen interface geometry during both the capillary condensation and evaporation processes.

A visual comparison of the hysteresis loops for VAL-21 and VFE−21 (Figure 2) shows that the addition of Fe resulted in about three times lower specific pore volume than that in the case of Al addition and a severe distortion

of the hysteresis loop. Such large pore volume and loop shape differences should also be reflected in surface area and PSD variations. The addition of La, though lower by 30% compared to Al and Fe additions, caused a pore volume reduction to an extent intermediate to those observed in the Al and Fe cases. The size (i.e. width) of the hysteresis loop is quite large, a fact reflected in the relatively high N_S value, $N_S = \sim20$ (Table 3).

The combined addition of La + Sr in a percentage equivalent to that for the exclusive addition of La has not affected the specific pore volume but caused a quite substantial change of the loop shape by lowering the adsorption isotherm and yielding an obviously different overall loop configuration. Such differences will be assessed via the relevant comparisons of key pore structure parameters.

The combined addition of La + Ce caused a significant pore volume reduction and loop shape distortion. Both changes compare well to those observed in the case of Fe addition despite the fact that the cumulative La + Ce addition was 30% lower than the Fe addition.

3.2. Modified Halsey and Kelvin Correlations. The successful CPSM simulation of nitrogen sorption hysteresis loops for MANPO materials portrayed in Figure 2 was obtained for the m and n values (i.e. parameters of the modified Halsey correlation (i.e. eq I-1) and Kelvin parameters $\cos\theta_c$ and $\cos\theta_h$ provided in Table 3. For the sake of visual comparison of the modified Halsey correlation used in this work to the original Halsey,[32] Lippens,[33] and Wheeler[34] correlations, the curves of Figure 3a were constructed. It is readily seen from the latter figure that the modified Halsey correlation (dashed curves in Figure 3a) compares satisfactorily with those reported in the literature.

By combining the modified Halsey and Kelvin correlations, the CPSM predicted P/P_0 versus D lines (dashed curves of Figure 3b) were drawn. The comparison of the CPSM lines with those reported by Broekhoff et al.[35] and Sonwane et al.[36] shows that the former predict lower pore sizes for a specified P/P_0 value. This observation can be

(32) Halsey, G. D. *J. Chem. Phys.* **1948**, *16*, 931.
(33) Lippens, B. C.; Linsen, B. G.; De Boer, J. H. *J. Catal.* **1964**, *3*, 32.
(34) Wheeler, A. *Catalysis;* Reinhold: New York, 1955; Vol. II, p 116.
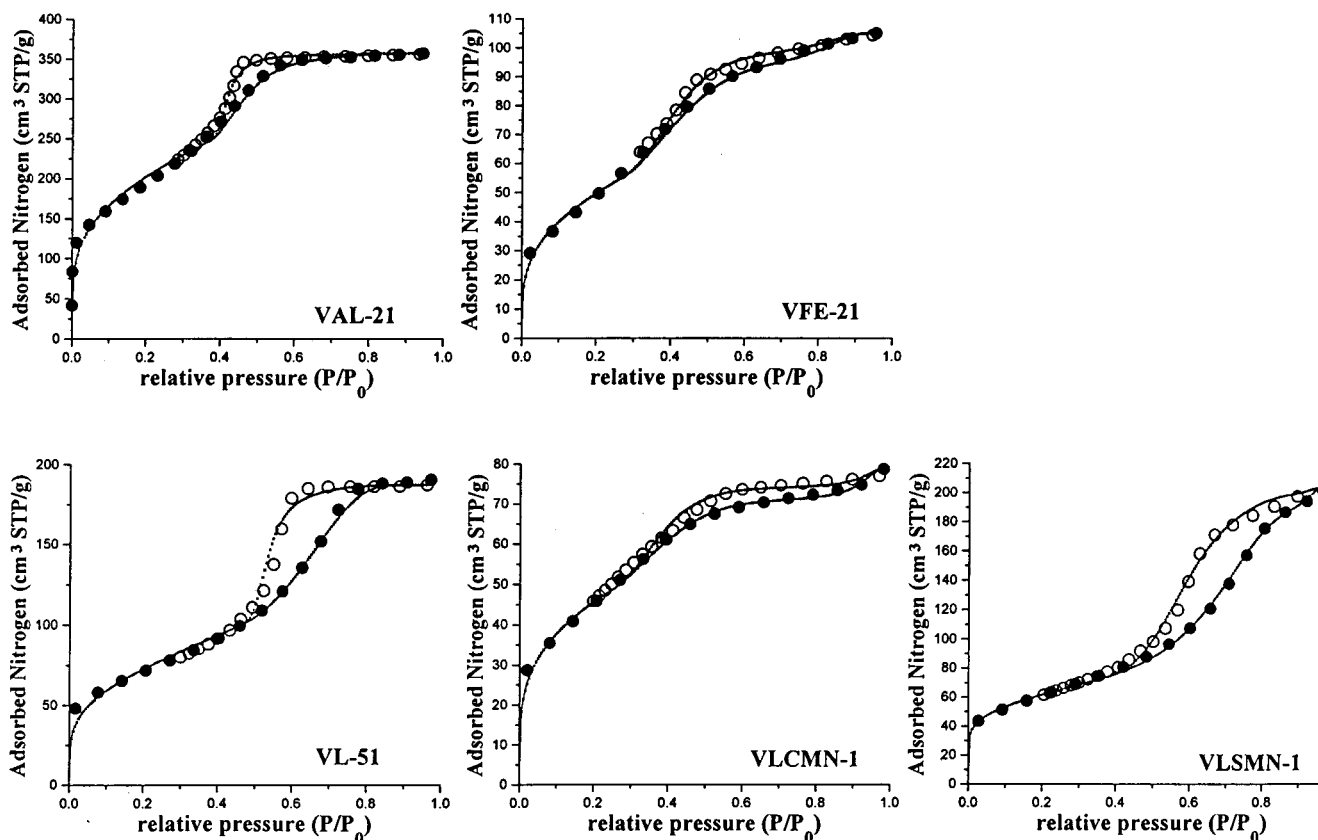
Figure 2. Nitrogen sorption hysteresis loops (77.4 K) of the MANPO samples of Table 1: (●) adsorption−capillary condensation; (○) desorption−capillary evaporation; (solid line) CPSM simulation (CPSM fitting parameters of Table 2).
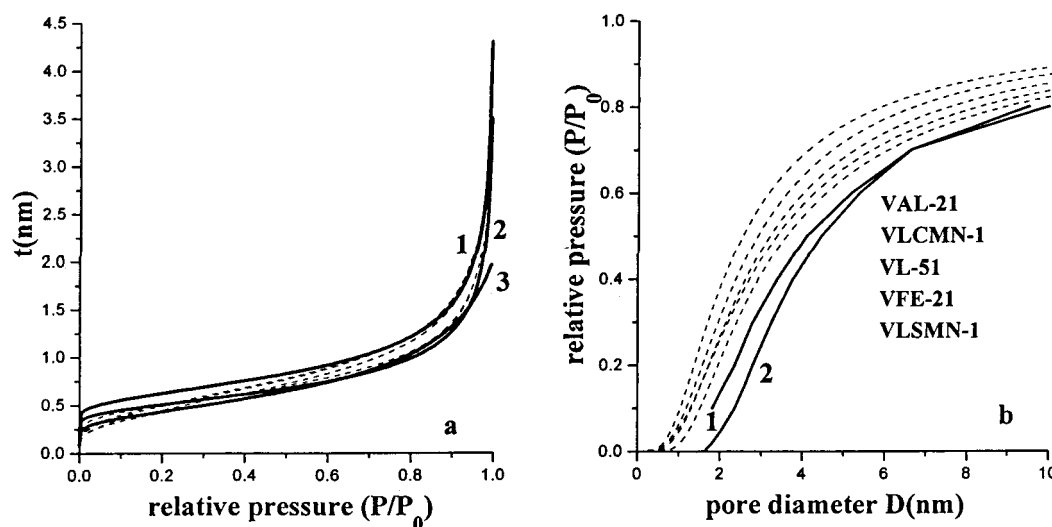

Figure 3. (a) Comparison of correlations for adsorbed monolayer thickness (t) versus P/P_0. Solid lines: (1) t (nm) = 0.35(5/ln-$(P_0/P))^{1/3}$;[34] (2) t (nm) = 0.43(5/ln$(P_0/P))^{1/3}$;[34] (3) data of Table 1.[33] Dashed curves: eq I-1 of this work, t (nm) = $n(5/\ln(P_0/P))^{1/3}(P/P_0)^m$, n and m values are provided in Table 2. (b) Comparison of P/P_0 versus pore size (D (nm)) plots. Solid lines reproduced from Figure 4:[33] (1) as proposed in ref 35; (2) as predicted by the molecular simulation model.[33] Dashed lines: derived in this work, by D (nm) = $[1.906/\ln(P_0/P)] \cos \theta + 2[n(5/\ln(P_0/P))^{1/3}(P/P_0)^m]$ for the cos θ, n, and m values provided in Table 3.

interpreted by considering the deviation of the liquid nitrogen meniscus geometry (i.e. cos θ < 1) from the identical hemispherical geometry (i.e. cos $\theta = 1$, eq 11[18]). Values of cos θ just below cos $\theta = 0.5$ indicate the presence of limited microporosity.

3.3. Pore Surface Area. Specific surface areas (SSAs) for the MANPO samples were determined by applying the two BET variants for multilayer and monolayer

adsorption as proposed in the original citation.[14] BET plots are provided in Figure 4 whereas the relevant numerical data together with the corresponding P/P_0 range for BET linearity as well as values for the C_{BET} constant are given in Table 4. These surface areas are in general considerably higher than those reported by Tian et al.[11] (i.e. 59−170 m²/g) for manganese oxide mesoporous solids (MOMs) fired at 600 °C. It is of special interest to note the high surface area (∼900 m²/g) of the VAL-21 sample that should be attributed to the presence of microporosity, which has

(35) Broekhoff, J. C. P.; De Boer, J. H. *J. Catal.* **1967**, *9*, 8.
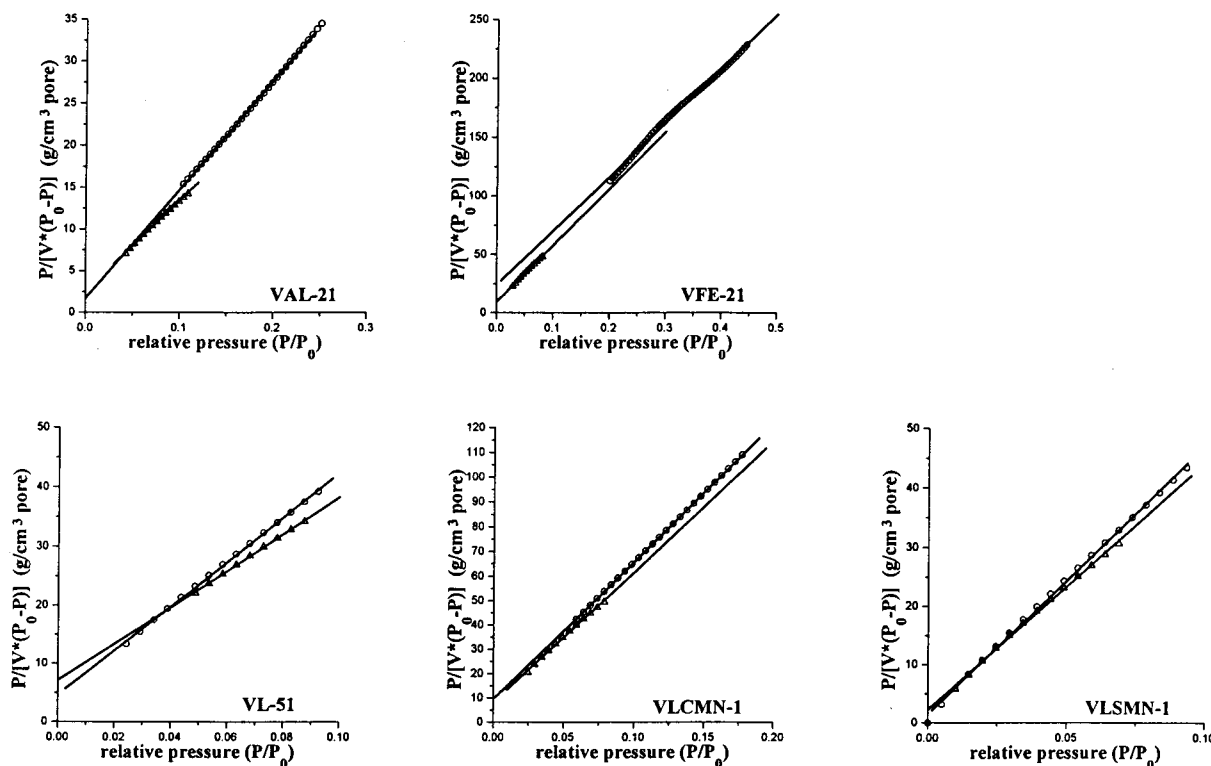(36) Sonwane, C. G.; Bhatia, S. K. *Chem. Eng. Sci.* **1998**, *53*, 3143.

Figure 4. BET plots for the manganese based materials of Table 1: (○) BET multilayer adsorption model;[19] (△) BET monolayer adsorption model.[19]

been detected from the CPSM simulation. The rest of the surface areas, depending on the BET variant applied, vary between 170 and 314 m²/g, well above the range 50–170 m²/g reported for the MOMs materials. In all cases the values of the C_{BET} constants for both BET procedures fall within acceptable limits, that is, $C_{BET} = \sim 20-200$. In the case of VFE–21, both BET variants predicted practically equivalent specific surface areas of about 200 m²/g.

Moreover, the BET SSA values are compared with the relevant CSSA obtained by the CPSM and the conventional Roberts method (Table 4). CPSM predictions are in perfect agreement with BET values (printed in bold in Table 4) while the respective Roberts values deduced for both the nitrogen capillary condensation and evaporation data are, in general, considerably lower (see percentages in parentheses of Table 4) than the BET predictions (i.e. printed in bold in Table 4). Furthermore, the CPSM predictions of CSSA for VAL-21 and VLCMN-1 samples agree with the BET-monolayer SSA values, a fact that is attributed to the presence of wider micropores (i.e. VAL-21) or mesopores of size approaching the upper limit (i.e. 2 nm) of the micropore region. This observation will become obvious via an inspection of the intrinsic PSDs.

3.4. Pore Volume and Surface Area Distribution. Pore volume and surface area PSDs in cumulative and differential form for all materials studied in this work are available in electronic form (Supporting Information). Both the CPSM and the Roberts method predict bimodal intrinsic pore size distributions for the MANPO materials studied in this work. However, the Roberts method predicts PSDs located over a higher pore size range than those of the CPSM and the pertinent CSSAs are considerably lower than the corresponding BET pore surface areas, while CPSM CSSA predictions are in perfect agreement with the relevant BET values.

CPSM intrinsic PSD parameters are provided in Table 3. CPSM derived intrinsic differential PSDs for the MANPO materials are presented in Figure 5. It is obvious

from Figure 5a1 and b1 that the addition of La created a PSD located over the approximate range 3–20 nm while the addition of Al and Fe gave rise to an intrinsic PSD practically extending over the range 2–12 nm. A comparison of the intrinsic PSD for MANPO solids containing La (Figure 5a2 and b2) reveals that the combined addition of La + Ce results in a shift of the intrinsic PSD toward the micropore region (i.e. 1.8–6 nm), while the La + Sr addition does not cause any PSD shift compared to the PSD valid for the sample possessing exclusively La (i.e. 3–9 nm).

3.5. Mean Hydraulic Pore Diameters. Mean hydraulic pore diameters, $D_{mh} = 4 V_p/S_{BET}$, were computed for all MANPO samples by considering both BET surface area estimates for each particular sample. The relevant results are reported in Table 5. Generally, D_{mh} values are lower (i.e. by 0–40%) than the respective CPSM predictions and more or less equal to the mean pore diameter of ∼3 nm reported by Tian et al.[11] for the MOMs materials.

3.6. Tortuosity Factor Predictions. Tortuosity factors for the materials under examination were computed from the empirical correlation of eq I-6 in the Appendix (i.e. CPSM–tortuosity[24]), and the relevant values are shown in Table 5. The latter values vary over the approximate range $\tau_{CPSM} = 2.96-5.70$ and are typical of porous catalysts that usually show tortuosity factors between 3 and 10.[37] The CPSM predicted tortuosity factors for the MANPO materials are higher than those (i.e. $\tau_{CPSM} = 1-2.35$) obtained by the same model for MCM-41 materials.[37] The latter observations indicate that unlike the highly ordered mesoporous MCM-41 materials the MANPO samples possess a relatively more complex pore structure.

3.7. Material Catalytic Performance Observations. We emphasize the fact that such MANPO materials are

(37) Salmas, C. E.; Stathopoulos, V. N.; Pomonis, P. J.; Rahiala, H.; Rosenholm, J. B.; Androutsopoulos, G. P. *Appl. Catal., A* **2001**, *216*, 23.
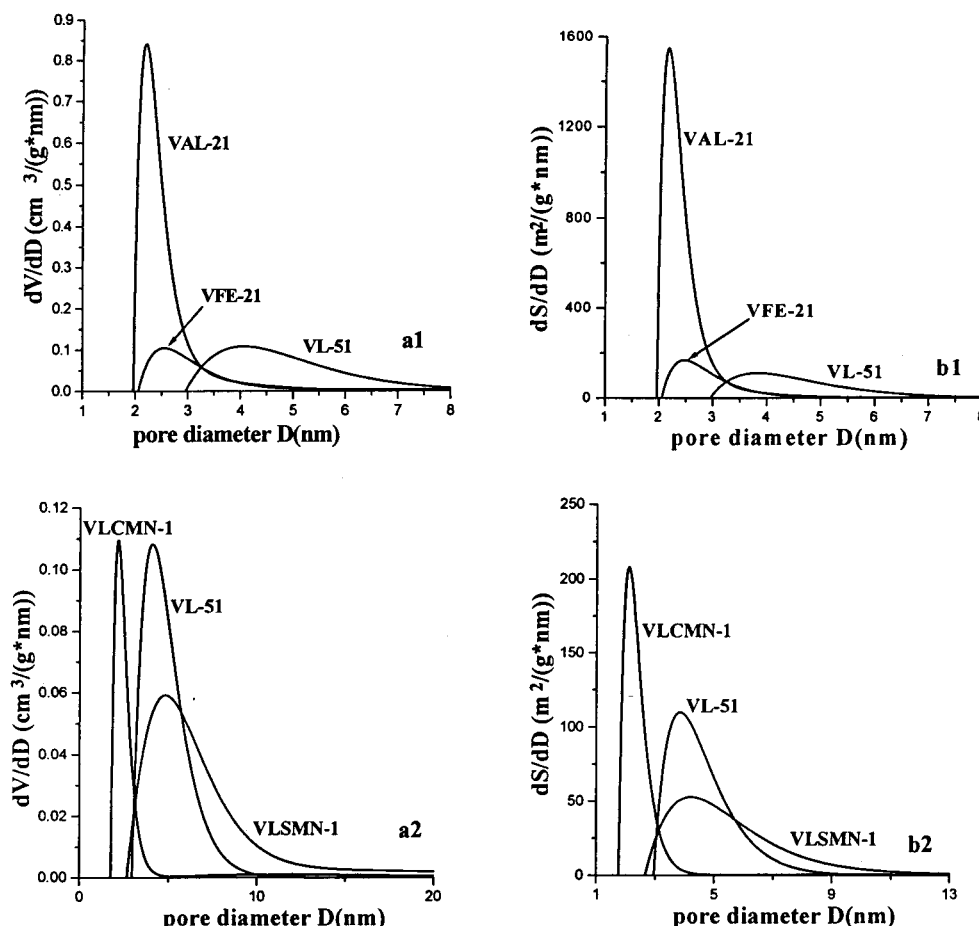
Figure 5. Comparison of CPSM predicted intrinsic pore size frequency distributions (PSDs).

Table 5. Tortuosity Factor Data for Manganese Based Mesoporous Materials As Predicted by the CPSM–Tortuosity Model[24]

specimen	N_s	$D_{min,eff}$ (nm)	$D_{max,eff}$ (nm)	D_{mean} (nm)	τ_{CPSM}	V_p, pore volume (cm^3/g)	mean hydraulic pore diameter, D_p (nm)	
							$4V_P/S_{BET(mu)}$	$4V_P/S_{BET(mo)}$
VAL-21; Mn/Al = 0.85	10	2.02	4.45	**2.55**	3.19	0.55	2.97	**2.44**
VFE−21; Mn/Fe = 0.85	3.2	2.19	12.52	**4.04**	2.96	0.16	**3.18**	**3.17**
VL=51; Mn/La = 1.70	20	3.2	8.10	**4.90**	4.66	0.29	**4.62**	3.69
VLCMN-1; Mn/La/Ce = 0.85:0.5:0.5	3.4	1.86	21.10	**4.20**	4.80	0.12	2.82	**2.62**
VLSMN-1; Mn/La/Sr = 0.85:0.5:0.5	6	3.2	27.40	**7.98**	5.70	0.32	**6.04**	5.52

Table 6. Catalytic Performance of Various Catalysts toward the CH$_4$/NO/O$_2$ Lean-NO$_x$ Reaction in the Range 200−350 °C

catalyst (mmol·g$_{cat}$·s^{-1})	experimental conditions (%)	T (°C)	rate N$_2$ ($\times$ 10^2)	S_{N_2}	ref
1 wt % Pt/SiO$_2$	500 ppm NO/1000 ppm CH$_4$ 1000 ppm O$_2$/He, GHSV = 60 000 h^{-1}	270	9.70	n.a.	40
1 wt % Rh/Al$_2$O$_3$	2000 ppm NO/6700 ppm CH$_4$/ 5% O$_2$, GHSV = 20 000 h^{-1}	200 350	0.08 0.60	80 86	31
Mn−La−Sr−Ce−O	2000 ppm NO/6700 ppm CH$_4$/ 5% O$_2$, GHSV = 12 000 h^{-1}	200 300	1.70 2.00	98 80	31, 39

very effective catalysts for redox reactions, such ase lean NO$_x$ reduction in a NO/CH$_4$/O$_2$ reaction mixture.[31,39] Table 6 compares the results obtained for the best catalysts reported for the NO/CH$_4$/O$_2$ lean NO$_x$ reaction in the low-temperature range 200−350 °C and a MANPO solid. Even though the comparison is not based on exactly the same reaction conditions, useful conclusions can be drawn. The Pt/SiO$_2$ catalyst shows a maximum reaction rate at 270 °C with a value about five times higher than that observed on the present MANPO solid. However, the former catalyst

was reported to lose its activity drastically by increasing the oxygen concentration beyond 0.1 mol %, while its activity versus temperature profile appears as a sharp peak. The latter behavior is just opposite to that obtained on the present MANPO solid.

4. Conclusions

The preparation of manganese based mesoporous materials (MANPOs) having high surface areas (i.e. 180−900 m^2/g) was accomplished. The latter values are higher than those reported for manganese oxide mesoporous solids (i.e.59−170 m^2/g).

The corrugated pore structure model (CPSM−nitrogen) is a quite flexible analytical tool for successful simulations

(38) Washburn, E. W. *Proc. Natl. Acad. Sci.* **1921**, *7*, 115.
(39) Stathopoulos, V. N.; Costa, C.N.; Pomonis, P. J.; Efstathiou, A. M. *Top. Catal.* **2001**, *16/17*, 231.
(40) Burch, R.; Ramli, A. *Appl. Catal., B* **1998**, *15*, 63.

of nitrogen sorption hysteresis loops obtained for MANPO materials. The CPSM through the best fit of the sorption hysteresis data enabled the evaluation of intrinsic pore size distributions, the prediction of working Halsey and Kelvin correlations, the detection of microporosity, and the evaluation of cumulative pore surface areas in perfect agreement with BET theory estimates. The CPSM−tortuosity variant was applied in realistic evaluations of pore structure tortuosity factors.

The Roberts method, taken as the most appropriate representative of the conventional procedures for PSD computation, predicted cumulative specific pore surface areas substantially lower than the pertinent BET values, irrespective of the chosen sorption hysteresis branch. The Roberts method and similar methods provide neither for the detection of microporosity nor for the evaluation of tortuosity factors.

The tortuosity factors for the MANPO materials, in the approximate range $\tau_{CPSM} = 3-5.7$, were predicted by the CPSM−tortuosity model. These values are typical of conventional porous catalysts and indicate that the MANPO materials possess a complex pore structure in contrast to the highly ordered pore structure of MCM-41 solids (i.e. $\tau_{CPSM} = 1-2.35$).

Mean CPSM predicted pore diameters are clearly and systematically greater than the respective mean hydraulic pore diameters of the MANPO materials as well those reported in the literature for the manganese oxide mesoporous solids (MOMs).

MANPO materials are very effective catalysts for redox reactions, such as the lean NO_x reduction in $NO/CH_4/O_2$ reaction mixtures.

Nomenclature

D = pore diameter (nm)

D_{AB} = binary diffusivity of two counterdiffusing species A and B, through a straight cylindrical pore of mean diameter D_{mean}

D_m = molecular diffusivity of gaseous systems

D_C, D_h = diameter of pore filled up with condensate through a cylindrical or a hemispherical l/v interface shape, (nm)

D_e = effective diffusion coefficient based on the cross-sectional area of a homogeneous porous particle

D_K = Kelvin core diameter (nm) (i.e. eq. I-2) or Knudsen diffusivity (eq 6)

D_{min}, D_{max} = minimum and maximum pore diameter detected by nitrogen condensation (nm)

$D_{min,eff}$, $D_{max,eff}$: as defined by eq I−7

D_{mean} = mean pore diameter as predicted by the intrinsic pore size distribution

D_{mh} = mean hydraulic pore diameter, $D_{mh} = 4V_p/S_{BET}$.

$f_i(b_i;D)$ = component pore number distribution function (eq III-2) of BSD type used in the synthesis of $F(D)$

$F(D)$ = intrinsic pore number distribution density function, as defined by eq III-1

$F_V(D) = D^2 F(D)$

J_i = diffusion flux of species i (mol/(m² s))

m = exponent in eq I-1

M_i = molecular weight of species i

n = multiplication factor in eq I-1 (monolayer thickness)

n_a = amount of gas adsorbed at relative pressure P/P_0 (μmol/g)

n_m = monolayer capacity (μmol/g)

N_S = number of pore segments forming a corrugated pore (also nominal pore length)

P/P_0 = relative gas pressure

P_j = probability for at least one l/v hemispherical interface to be adjacent to the general jth segment of a corrugated pore[17]

q = probability for a pore segment of size D_j to be within the range D_h-D_{max}[17]

t = thickness of physically adsorbed nitrogen multilayer (nm)

T = temperature (K)

V_{ads} = relative saturation during capillary condensation

V_{der} = relative pore volume evacuated by desorbed−evaporated nitrogen (eq I-5)

V_p = specific pore volume (cm³/g)

V_{sr} = relative saturation during capillary evaporation ($1 - V_{der}$)

Y_i = mole fraction of component i

Acronyms

BSD = bell shaped distribution function: $(D - D_{min})(D - D_{max}) \exp(bD)$

CPSM = corrugated pore structure model

CSSA = cumulative specific surface area

PSD = pore size distribution

SSA = specific surface area

Greek Letters

ϵ = porosity ($V_{pore}/V_{particle}$)

θ_C, θ_h = liquid nitrogen contact angles for cylindrical and hemispherical liquid nitrogen meniscuses, respectively

τ = tortuosity factor = $\epsilon D_{AB}(D_{mean})/D_e$ eq 3 (dimensionless)

τ_{CPSM} = tortuosity factor as defined by eq I-6

Appendix I

Adsorbed Nitrogen Statistical Multilayer Thickness. A modified Halsey equation[17,18] that has been tested by carrying out various applications, concerning the curve fitting of adsorption data of various materials, is also used in the present work,

$$t = n[5/\ln(P_0/P)]^{1/3}(P/P_0)^m \tag{I-1}$$

where $n = 3.5-4.3$ and $m = 0-0.1$ (for [t] in angstroms).

Kelvin Equation. The version of the Kelvin equation[17,18] to be used in the hysteresis loop simulations using the CPSM is shown in eq I-2,

$$D_K = [1.906/\ln(P_0/P)] \cos \theta \tag{I-2}$$

where D_K is the Kelvin diameter (nm) and θ is the nitrogen liquid−vapor interface contact angle ($\cos \theta = 0.5$ for a cylindrical interface geometry, $\cos \theta = 1.0$ for a hemispherical interface geometry). Any $\cos \theta$ value between 0.5 and 1.0 stands for the intermediate liquid nitrogen meniscus geometry whereas values of $\cos \theta$ lower than 0.5 indicate an arbitrary interface geometry and the presence of microporosity.

CPSM−Nitrogen Model. *Adsorption−Capillary Evaporation Isotherm.* The relative volume V_{ads} of gas adsorbed at a specified relative pressure can be computed via eq I-3.

$$V_{ads} = [1/\int_{D_{min}}^{D_{max}} D^2 F(D) \, dD]\left[4t\int_{D_h}^{D_{max}}(D - t)F(D) \, dD + \right.$$

$$\int_{D_{min}}^{D_C} D^2 F(D) \, dD + \int_{D_C}^{D_h} D^2 F(D) \, dD\left(\frac{1}{N_S}\sum_{j=1}^{j=N_S}(P_j)\right) +$$

$$\left.4t\int_{D_C}^{D_h}(D - t)F(D) \, dD\left(\frac{1}{N_S}\sum_{j=1}^{j=N_S}(1 - P_j)\right)\right] \tag{I-3}$$

Desorption−Capillary Evaporation Isotherm. The relative amount of nitrogen evaporated and/or desorbed, V_{der}, as a function of the relative gas pressure can be evaluated via eq I-5 while the fraction of the pore volume, V_{sr}, saturated with nitrogen is given by eq I-4.

$$V_{sr} = 1 - V_{der} \qquad (I\text{-}4)$$

$$V_{der} = \int_{D_h}^{D_{max}} (D - 2t)^2 F(D)\, dD \left(\frac{2}{N_S} \frac{1 - q^{N_S}}{1 - q} - q^{N_S - 1} \right) / \int_{D_{min}}^{D_{max}} D^2 F(D)\, dD \quad (I\text{-}5)$$

Proof of eqs I-3 and I-5 is presented elsewhere.[17]

CPSM−Tortuosity Model. The CPSM−nitrogen theory has been utilized in the formulation of an empirical correlation that predicts tortuosity factors; thus,

$$\tau_{CPSM} = 1 + 0.69 \left(\frac{D_{max,eff} - D_{min,eff}}{D_{mean}} \right) (N_S - 2)^{0.58} \quad (I\text{-}6)$$

where $D_{max,eff}$ and $D_{min,\,eff}$ are calculated from

$$\int_{D_{max,eff}}^{D_{max}} Fv(D)\, dD = \int_{D_{min}}^{D_{min,eff}} Fv(D)\, dD = 0.025 \quad (I\text{-}7)$$

or

$$\int_{D_{max,eff}}^{D_{max}} D^2 F(b;D)\, dD = \int_{D_{min}}^{D_{min,eff}} D^2 F(b;D)\, dD = 0.025 \quad (I\text{-}8)$$

Details of the CPSM−tortuosity theory are given in ref 24.

Appendix II

CPSM−Mercury Model. The Wahburn equation reads

$$P = -4\gamma \cos\theta / D \qquad (II\text{-}1)$$

where P is the applied pressure, D is the pore diameter, γ is the surface tension, and θ is the contact angle of mercury.[38]

Mercury Penetration. The CPSM prediction of the intruded mercury volume as a function of the applied pressure reads

$$V_P(P(D)) = \frac{A}{k} \left(\int_D^{D_{max}} D^2 F(D)\, dD / \int_{D_{min}}^{D_{max}} D^2 F(D)\, dD \right) \quad (II\text{-}2)$$

where

$$A = (1 - P_S^{2k})/(1 - P_S) - kP_S^{2k-1} \quad \text{for} \quad P_S < 1$$

or

$$A = k \quad \text{for} \quad P_S = 1$$

and

$$P_S = \int_D^{D_{max}} F(D)\, dD$$

Mercury Retraction. The CPSM prediction of the volume of mercury withdrawn (i.e. V_W), under decreasing pressure conditions, can be computed from the following equations:

Case i: for $D_{min} < D < (D_{min}/\lambda)$

$$V_W(P(D)) = \left(\frac{B}{2k^2} / \int_{D_{min}}^{D_{max}} D^2 F(D)\, dD \right) \int_{D_{min}}^{D} D^2 F(D)\, dD \quad (II\text{-}3)$$

Case ii: for $(D_{min}/\lambda < D < D_{max}$

$$V_W(P(D)) = \left(\frac{B}{2k^2} / \int_{D_{min}}^{D_{max}} D^2 F(D)\, dD \right) [\int_{D_{min}/\lambda}^{D} (D^2 F(D) \int_{D}^{D_{max}} F(D)\, dD)\, dD + \int_{D_{min}}^{D_{min}/\lambda} D^2 F(D)\, dD] \quad (II\text{-}4)$$

where

$$B = (2k/(1 - P_C)) - ((1 - P_C^{\,k})(P_C + P_C^{\,k}))/(1 - P_C^{\,2}) \quad \text{for} \quad P_C < 1$$

or

$$B = 2k^2 \quad \text{for} \quad P_C = 1 \quad \text{and} \quad P_C = 1 - P_S$$

The CPSM predicted mercury retraction line is deduced from the following equation:

$$V_R = (1 - V_W) \qquad (II\text{-}5)$$

Proof of eqs (II-2)−(II-5) is presented elsewhere.[25]

Appendix III: Intrinsic Pore Segment Number Distribution Function

The normalized $F(D)$ in its general form (i.e. composed of n unimodal PSDs) reads

$$F(D) = \sum_{r=1}^{r=n} \left(\frac{w_r}{R_r} \right) \frac{f_r(b_r;D)}{\Phi_r} / \sum_{r=1}^{r=n} \left(\frac{w_r}{R_r} \right) \quad (III\text{-}1)$$

where w_r is the weight of a unimodal PSD,

$$\sum_{r=1}^{r=n} w_r = 1$$

$$f_r(b_r;D) = (D - D_{min})(D - D_{max}) \exp(bD) \quad (III\text{-}2)$$

$$\Phi_r = \int_{D_{min}}^{D_{max}} (D - D_{min})(D - D_{max}) \exp(bD)\, dD \quad (III\text{-}3)$$

where Φ_r is the normalization factor of $f_r(b_r;D)$ and

$$R_r = \int_{D_{min}}^{D_{max}} D^2 \left(\frac{f_r}{\Phi_r} \right) dD$$

is the normalization factor of each one of the pore volume distributions composing the overall pore volume distribution.